remote sensing

MDPI

Article

Study of PBLH and Its Correlation with Particulate Matter from One-Year Observation over Nanjing, Southeast China

Yawei Qu [1], Yong Han [1,2,*], Yonghua Wu [3], Peng Gao [1] and Tijian Wang [1]

1 School of Atmospheric Sciences, Nanjing University, Nanjing 210023, China; yawei_qu531@163.com (Y.Q.); 13813373839@163.com (P.G.); tjwang@nju.edu.cn (T.W.)
2 School of Atmospheric Sciences, Sun Yat-sen University, Guangzhou 510275, China
3 NOAA-CREST, City College of the City University of New York, New York, NY 10031, USA; yhwu@ccny.cuny.edu
* Correspondence: HanYong@nju.edu.cn; Tel.: +86-25-89681159

Received: 29 April 2017; Accepted: 23 June 2017; Published: 28 June 2017

Abstract: The Planetary Boundary Layer Height (PBLH) plays an important role in the formation and development of air pollution events. Particulate Matter is one of major pollutants in China. Here, we present the characteristics of PBLH through three-methods of Lidar data inversion and show the correlation between the PBLH and the $PM_{2.5}$ ($PM_{2.5}$ with the diameter <2.5 μm) in the period of December 2015 through November 2016, over Nanjing, in southeast China. We applied gradient method (GRA), standard deviation method (STD) and wavelet covariance transform method (WCT) to calculate the PBLH. The results show that WCT is the most stable method which is less sensitive to the signal noise. We find that the PBLH shows typical seasonal variation trend with maximum in summer and minimum in winter, respectively. The yearly averaged PBLH in the diurnal cycle show the minimum of 570 m at 08:00 and the maximum of 1089 m at 15:00 Beijing time. Furthermore, we investigate the relationship of the PBLH and $PM_{2.5}$ concentration under different particulate pollution conditions. The correlation coefficient is about −0.70, which is negative correlation. The average PBLH are 718 m and 1210 m when the $PM_{2.5} > 75$ μg/m^3 and the $PM_{2.5} < 35$ μg/m^3 in daytime, respectively. The low PBLH often occurs with condition of the low wind speed and high relative humidity, which will lead to high $PM_{2.5}$ concentration and the low visibility. On the other hand, the stability of PBL is enhanced by high PM concentration and low visibility.

Keywords: planetary boundary layer; $PM_{2.5}$; air pollution; Lidar

1. Introduction

In recent years, with the acceleration of urbanization and industrialization, air pollution is becoming more and more serious in China [1,2]. Fine Particulate Matter (PM) has become one of major pollutants because they can be inhaled into human body by respiration, resulting in various respiratory and cardiovascular disease [2]. Meanwhile, they can directly scatter and absorb solar radiance and indirectly modify cloud properties [3–6], thus, play an important role in Earth's energy budget, climate change and atmospheric environment. The PM concentration level also affects the stability of planetary boundary layer (PBL) [7,8]. Different numerical models and measurements have been applied to investigate the radiative forcing of nitrate [9], sulfate [10,11], and carbonaceous aerosols [12,13], as well as their mixtures [14–17] over East Asia. These studies demonstrated that aerosol particles can reduce the solar radiation reaching ground and augment the planetary albedo. The negative radiative forcing and cooling effects of aerosols in lower PBL and ground can suppress the development of PBL.

On the other hand, the concentration of aerosols is strongly affected by the meteorological conditions [18–20] and the PBLH plays an important role [21]. PBL is a strongly turbulent layer

between earth's surface and free troposphere. The PBLH can weaken the exchange between boundary layer and free troposphere, because weak turbulence will occur in the bulk of the atmosphere due to the stable stratification between different layers [22]. Air pollutants released from non-buoyant ground sources, including aerosols, dust and other gaseous pollutants, are restricted within the boundary layer [23]. Therefore, the dispersion and transport of lower tropospheric particles mainly depend on the PBLH [24,25].

Consequently, the determination of PBLH is important to evaluate air-pollution events. The PBLH can be calculated from remote sensing observations methods, including satellite [26,27], wind profiler [28], ceilometer [29–31], sodar [32,33] and ground-based Lidar [34–37]. Lidar can provide continuous measurements with highly temporal-spatial resolution, and the continuous automatic inversion of PBLH from Lidar data is more feasible. Several methods have been employed to calculate the PBL height by using Lidar data, such as the gradient method [38–41], standard deviation method [42,43], wavelet analyses [44–46], and idealized profiles method [47,48]. Due to the big variation of aerosol concentration in boundary layer and free troposphere, the fundamental principle of these methods is to extract the height where the largest Lidar signal variance (i.e., strongest decrease of the backscatter signal) appears. However, each method has its own limitations (e.g., susceptible to noise and stratified aerosol structures). To our best knowledge, the study of multi-methods estimate of PBLH and the correlation between PBLH and $PM_{2.5}$ in Yangtze River Delta (YRD) is insufficient. In particular, the research on the $PM_{2.5}$–PBLH interaction helps better understand air pollution process and mechanism; this becomes very important for the severe haze episodes in the urban cities of China [8,20,23].

Here, we present a study of the PBLH variations and the correlation between PBLH and $PM_{2.5}$ by inversing PBLH through three different ways. The Lidar data were collected during December 2015–November 2016 in Nanjing, one of the megacities in YRD, China. Section 2 introduces the observation settings and the inversion methods, including the gradient method, standard deviation method and wavelet covariance transform method. In Section 3, we compare the PBLH calculated by different methods, show the characteristics of seasonal and diurnal PBLH variations, and further discuss the relationship between PBLH and $PM_{2.5}$ through statistics on one-year data and a case study. Finally, the conclusion and perspective are given in Section 4.

2. Materials and Methods

2.1. Observation

The LIDAR backscatter signal profile and the inversion for PBLH were carried out during December 2015–November 2016 in Nanjing, west part of Yangtze River Delta, China. A Raman Lidar system (LR112-D400) manufactured by Raymetrics of Greece was used at Atmospheric Parameters Vertical Detection Site (APVDS) in Nanjing University Xianlin Campus (32.12°N, 118.95°E). The Lidar system is based on a pulsed Nd:YAG laser, which transmits short pulses at 355 nm with a 10 Hz repetition rate and the maximum output energy of 85 mJ. The optical receiver is a Cassegrain telescope with 400 mm diameter and a field of view of 1.75 mrad. Four receiving channels are used to collect elastic scattering and polarization signals (355 parallel and 355 perpendicular channels) and Nitrogen (N_2) Raman scattering signals at 387 nm and water vapor Raman-scattering at 408 nm, respectively. The maximum detection height and minimum vertical resolution are 18 km and 7.5 m, respectively. The Lidar overlap area is around 255 m. The Lidar system worked in the rainless daytime during the one-year period. Due to the limitation of weather conditions and lack of operators, 63 days of effective samples were collected. The observational data covers 10 months of four seasons in Nanjing, including winter (December 2015–January 2016–February 2016), spring (March 2016–April 2016–May 2016), summer (June 2016–August 2016) and autumn (September 2016–November 2016), respectively. Lidar profiles obtained in this study are averaged over 4 min, which matches the typical time scale of atmospheric turbulence within the boundary layer [22].

The $PM_{2.5}$ concentration and visibility were measured at Xianlin Ambient Air Quality Monitoring Site (XAAQMS), which is located on the Xianlin Campus of Nanjing Normal University (32.11°N, 118.92°E) and only 4 km away from the APVDS. A continuous ambient particulate monitor (Thermo TEOM-1405) was used for the $PM_{2.5}$ measurement and the hourly-average data were collected. Meteorological parameters including temperature, relative humidity and wind speed over the same period were provided by the National Meteorological Station of Nanjing (NMSN ID: 58238, 32.00°N, 118.80°E). The location of APVDS, XAAQMS, and NMSN are shown in the map of Nanjing in Figure 1.

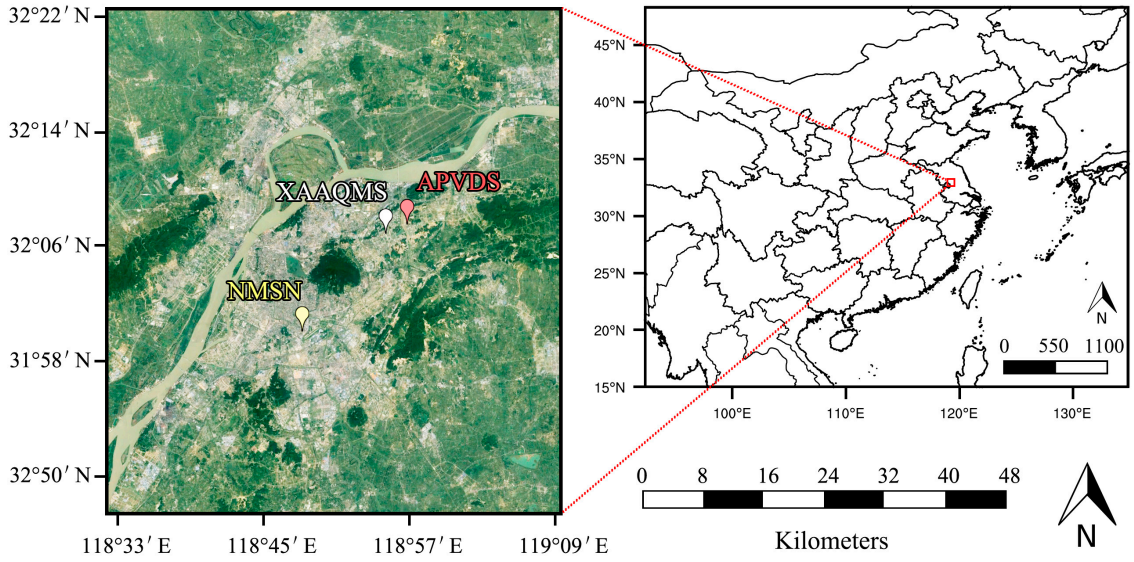

Figure 1. Map of Nanjing, China and the location of observation sites including APVDS (32.12°N, 118.95°E), XAAQMS (32.11°N, 118.92°E), and NMSN (32.00°N, 118.80°E).

2.2. Inversion of Backscatter Coefficient by Lidar

The Lidar equation [35] can be expressed as:

$$P(R) = P_0 \frac{c\tau}{2} An \frac{O(R)}{R^2} \beta(R) exp[-2\int_0^R \alpha(r)dr], \quad (1)$$

where $P(R)$ is the power received from a distance R and P_0 is the average power of a single laser pulse. τ is the temporal pulse length, A is the area of primary receiver optics, n is the overall system efficiency and $O(R)$ is the overlap function. $\beta(R)$ and $\alpha(r)$ represent backscatter coefficient and extinction coefficient, respectively.

The Lidar equation in this paper is solved by using the Klett–Fernard method [49]. Backscatter coefficient can be calculated through following equation:

$$\beta(R) = \frac{RCS(R) \cdot exp[2(L - L_{mol}) \int_R^{R_{ref}} \beta_{mol}(r)dr]}{\frac{RCS(R_{ref})}{C\beta_{mol}(R_{ref})} + 2L \int_R^{R_{ref}} RCS(r\prime) \cdot exp[2(L - L_{mol}) \int_R^{R_{ref}} \beta_{mol}(r'')dr'']dr\prime}, \quad (2)$$

where $C = \frac{\beta_{mol}(R_{ref}) + \beta_{aer}(R_{ref})}{\beta_{mol}(r)}$, and β_{mol} and β_{aer} are backscatter coefficient of air molecules and aerosol, respectively. Reference point R_{ref} represents the clean atmosphere where $\beta_{aer}(R_{ref}) = 0$ and $C = 1$. The Range Corrected Signal (RCS) is defined as $RCS(R) = P(R)R^2$. $L = \frac{\alpha_{aer}(R)}{\beta_{aer}(R)}$ is the aerosol Lidar ratio and $L_{mol} = \frac{\alpha_{mol}(R)}{\beta_{mol}(R)}$.

2.3. Inversion of Planetary Boundary Layer Height

Aerosol is generally more abundant within the boundary layer than the upper atmosphere, thus for Lidar systems, the backscattered Lidar signals (e.g., RCS) within the PBL are much higher than that in the free troposphere. Based on this fact, several methods have been employed to determine the PBL height from Lidar data. In this study, we choose the GRA, WCT and STD method to estimate the PBLH where RCS abruptly decreases. The inversion methods are shown as follows:

The GRA method defines the position of the largest negative signal derivative ($D(z)$) as the instantaneous top of PBL or PBLH [37–41]. The $D(z)$ can be expressed as follows:

$$D(z) = \frac{dRCS}{dz}, \tag{3}$$

In the STD method, the PBLH is defined as the height of the maximum of Lidar signal variance [42,43]. The variance peaks of standard deviation (σ) are calculated from the variation in height of RCS, as follow:

$$\sigma = [\frac{1}{N}\sum_{i=1,N}\left(RCS_i - \overline{RCS}\right)^2]^{\frac{1}{2}}, \tag{4}$$

In WCT method [37,44–46], the conversion covariance function $W_f(a, b)$ is defined as:

$$W_f(a,b) = \frac{1}{a}\int_{z_b}^{z_t} RCS(z)h(\frac{z-b}{a})dz, \tag{5}$$

where z is the height, z_t and z_b are the upper and lower limits of RCS profiles, a is the spatial dilation of the function, and b is the translation of the Haar function, i.e., the central position of the Haar function. The Haar function (h) is defined as follows:

$$h\left(\frac{z-b}{a}\right) = \begin{cases} +1, \ b - \frac{a}{2} \le z < b \\ -1, \ b \le z < b + \frac{a}{2} \\ 0, \ elsewhere \end{cases}. \tag{6}$$

In this paper, z_b is set as 255 m where the Lidar starts to collect full backscatter signals due to the limitation of the geometric overlap function. z_t is set as 2500 m to save the computing time and cloud contamination; this will not cut off the true maximum PBLH because we first visually see aerosol distribution gradient from the Lidar images. As shown in supplementary Figure S1, both the PBLH results from lidar and radiosonde agree well. The spatial extent (a) of the function is 150 m. The WCT method evaluates the similarity between RCS and Haar function. The abrupt change in RCS will occur at the height where $W_f(a, b)$ reaches the maxima, and the PBLH can be determined accordingly.

3. Results and Discussion

3.1. Comparison between Three PBLH Calculation Methods

We applied three methods above to calculate the PBLH. Figure 2 presents the results of Lidar RCS profiles and PBLHs, as well as their daily variation on 17 January 2016. At first, Figure 2a illustrates three PBLHs at 11:50 when cloud covers the Lidar detective region. The PBLH inversion is sensitive to the backscatter signal of boundary layer clouds [40]. The GRA method determines the PBLH at 918 m at the lower layer of cloud. The other two methods locate the PBLH at the upper layer of cloud with the value of 1049 m and 1076 m for STD and WCT method, respectively. Figure 2b,c compares the variation of PBLH calculation within 8 min (17:32–17:40). PBLHs derived from the GRA and STD method change abruptly from 1215 m to 1025 m in such a short period, while the RCS profile and the PBLH derived from WCT method are almost unchanged. The nearly 200 m difference of PBLHs from GRA and STD methods may be contributing to the signal noise. The GRA and STD methods are more mutable and more sensitive to noise when comparing with WCT method, which can also

be observed in the diurnal variation in Figure 2d. Therefore, the WCT is the most stable method in PBLH determination. However, these methods are all able to show the variation of PBLH, which can be expressed as increasing in the morning and noon reaching, the maximum in the afternoon and decreasing after sunset. The average value of PBLH on 17 January 2016 is 1403 ± 156 m, and the PBLH from the above three methods are 1559 m, 1373 m and 1278 m for GRA, STD and WCT, respectively.

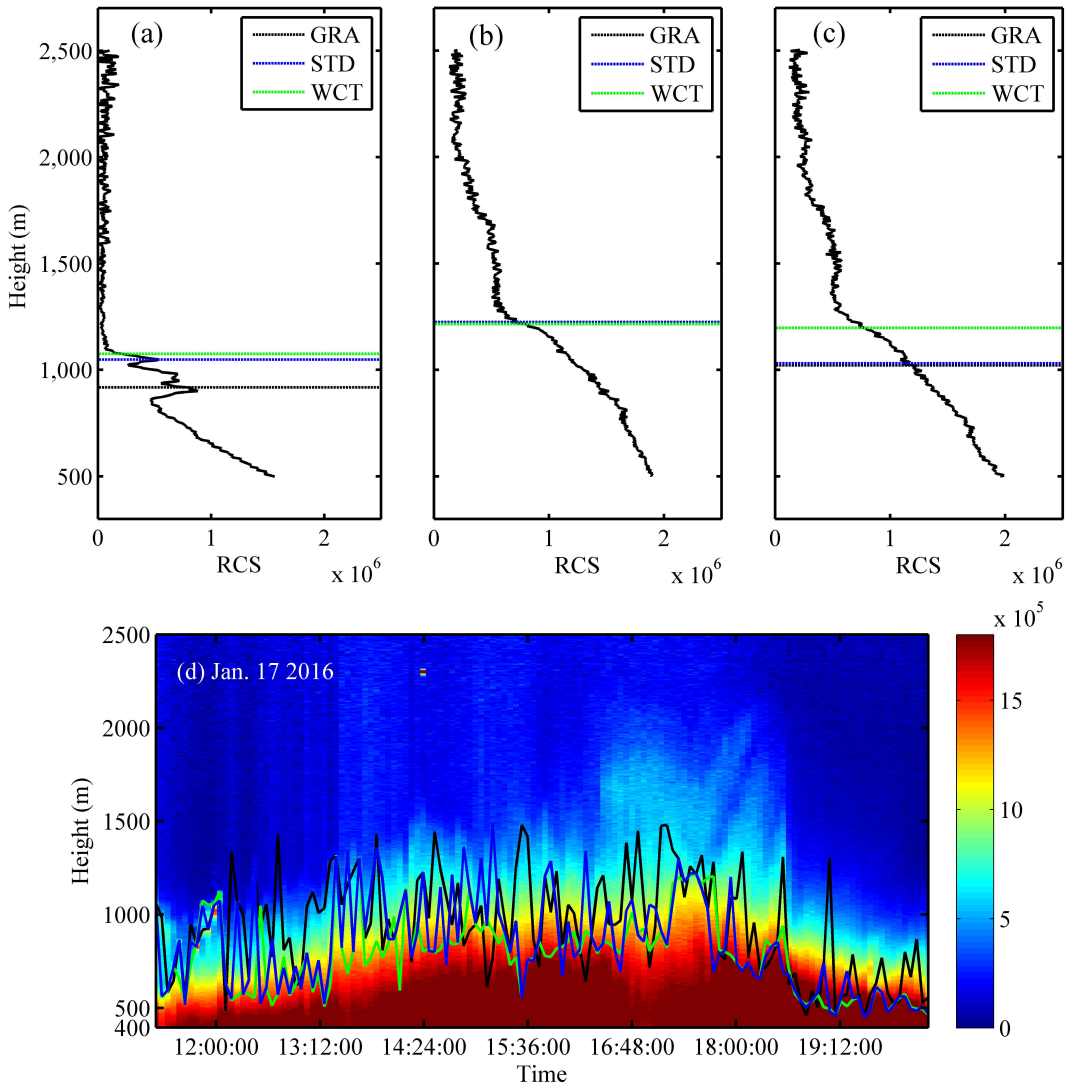

Figure 2. The RCS profile and PBLH at: 11:50 (**a**); 17:32 (**b**); and 17:40 (**c**) on 17 January 2016 and the diurnal variation of RCS and PBLH calculated by three methods (**d**) on 17 January 2016. The black, blue and green lines represent the PBLH calculated by GRA, STD and WCT, respectively.

3.2. PBL Statistical Characteristics

The PBLH generally shows seasonal and diurnal changes because of the variation in solar radiation, wind speed, atmospheric stability, etc. The following paragraphs will identify and discuss the statistical characteristics of PBLH over Nanjing.

The box plot in Figure 3 shows and compares statistical characteristics of PBLH seasonal variation, which is calculated by the GRA, STD and WCT methods and the average values of three methods. The figure reveals an annual variability of PBLH between 300 and 2433 m. Annual average boundary layer height is about 992 m, which is in good agreement with the experimental data in China [36,50] and is lower than the observational results from European countries [35,51]. The PBLH reaches lowest

in winter with 822 m on average, and has its highest value 1351 m in summer. The PBLH values in spring and autumn are similar with the value of 1051 m and 1096 m, respectively. Schneider et al. [51] and Matthias et al. [52] also found the annual cycle with a maximum in summer and a minimum in winter. The possible explanation can be given as the higher solar radiation and heat flux in summer lead to stronger surface heating and then stronger turbulence and convection [51].

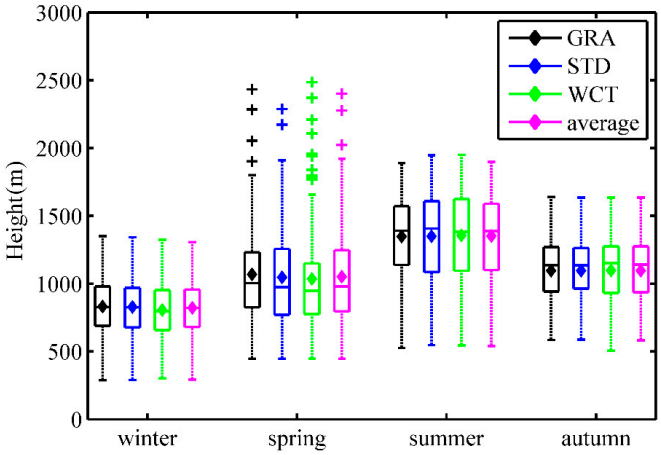

Figure 3. The seasonal variation of PBLH from the GRA, STD, and WCT methods, and their average of three above methods during one-year observation over Nanjing, China. The bottom and top of the box are the first and third quartiles, and the band inside the box is the median and the diamond is the average. The whisker is the lowest (highest) datum within 1.5 interquartile ranges (IQR) of the lower (upper) quartile, and data not included between the whiskers are plotted as an outlier with a plus.

The whiskers and outliers in Figure 3 show the variability in the PBLH in different seasons. It is clear that the PBLHs in winter are the most stable and have the minimum PBLH standard deviation (209 m). Though the maximum seasonal average PBLH is found in summer, the greatest variability of PBLH is found in spring with the standard deviation of 380 m. Spring is the only season with some outliers of PBLH and the maximum PBLH reaches 2433 m. Kamp et al. [53] found that the mean diurnal trend of PBLH in spring did not differ greatly from summer on clear days, while with the boundary-layer clouds the PBLH can be higher in spring than the one in summer. Thus, the variability in spring may be due to the existence of boundary-layer clouds. Considering the three different methods in seasonal PBLH inversion, the GRA method overestimates in winter and spring, and underestimates in summer and autumn, while WCT method shows an opposite trend with GRA in Figure 3. All three methods can reveal the characteristics of PBLH in different seasons.

Figure 4 depicts the hourly average PBLH and three-method average value of the PBL height and the related standard deviation during the daytimes (08:00–20:00). The diurnal cycle shows similar pattern in different seasons, which is generally minimum in the morning (08:00) and maximum in the afternoon. For annual average diurnal variation, the PBLH is 570 m at 08:00 and rises to a peak of 1089 m at 15:00. From 16:00 to 20:00, the annual average PBLH remains relatively stable and shows only a little lower after sunset, and finally decrease to 998 m at 20:00. The pattern in winter and spring are most similar to the annual cycle. The PBLH is kept at high level at 14:00 and 18:00 in summer, which leads to a two-peak pattern in this season. Strawbridge et al. [54] also observed the PBL peak at around 18:00–20:00 by using a Rapid Acquisition Scanning Aerosol Lidar (RASCAL) in August, 2001 in the Lower Fraser Valley (LFV) of British Columbia. The PBLH shows the greatest diurnal variations in summer and lowest in winter, which coincides with the results from Figure 3. The maximum among the year occurs at 15:00 in summer at 1554 m and the minimum occurs at 08:00 in winter at 552 m, respectively.

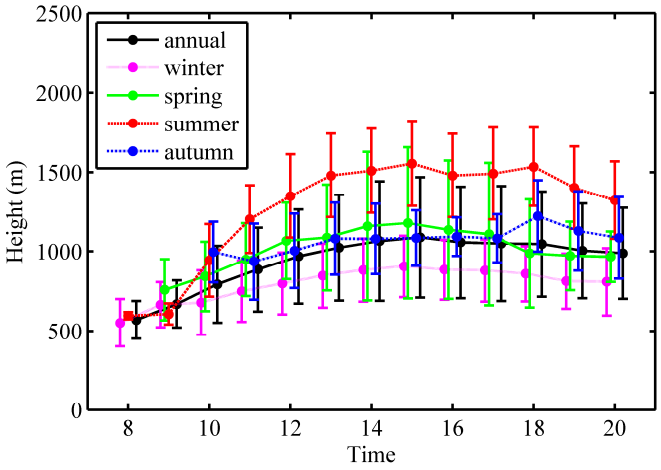

Figure 4. Diurnal variation of PBLH (three-method average) in different season observation in Nanjing, the error bar represents the standard deviation of each hour.

The error bar in Figure 4 represents the standard deviation of each hour. Therefore, larger error bars indicate more variability in PBLH, which is related to the more active convection within boundary layer. The standard deviation shows the greatest change in spring. The least stable PBLH can be found from 14:00 to 17:00 in spring, and the standard deviation is larger than 430 m. However, in the morning and evening of spring, the standard deviation is as low as 150 m. The diurnal variation of standard deviation resembles average PBLH; the higher the PBLH is, the larger the standard deviation is. This is possibly due to the strong turbulence and the weak stability of PBL [22]. The standard deviation is smaller than 210 m in winter's diurnal cycle, as the PBLH among four seasons, and winter PBL is the steadiest over the observation period.

3.3. PBLH Variation Properties under Different Particulate Pollution Conditions

In order to study the PBLH variation under different particulate pollution conditions, we classify the $PM_{2.5}$ concentration according to the new NAAQS of China. The air pollution level or category is often classified according to the $PM_{2.5}$ concentration. The NAAQS in China sets $PM_{2.5}$ concentration limits for 24-hour average with 35 $\mu g/m^3$ for Grade I and 75 $\mu g/m^3$ for Grade II [55]. Thus, in this study, three particulate pollution conditions are classified by the $PM_{2.5}$ concentrations levels as follows: (1) *good* condition, with $PM_{2.5}$ concentration less than 35 $\mu g/m^3$; (2) *slightly polluted*, with $PM_{2.5}$ concentration betwee 35 $\mu g/m^3$ and 75 $\mu g/m^3$; and (3) *polluted*, with $PM_{2.5}$ concentration exceeding 75 $\mu g/m^3$. We assume that the human-made emissions very little in Nanjing under the same season or month. We also exclude the data when the significant variations of weather or climate occur.

Figure 5 compares the PBLH calculated by the GRA, STD and WCT methods and the average of 3 methods under *the good*, *slightly polluted*, and *polluted* conditions. PBLH is relatively lower in *polluted* condition than that in *good* condition, and the average PBLH is 718 m and 1210 m, respectively. In *slightly polluted* days, the height of PBL is moderate with the value of 1027 m. Very high daytime average PBLH values can appear under *good* condition, however, the lowest value occurs under *slightly polluted* condition, though exceeds the 1.5 IQR. Moreover, the very low values of daytime average PBLH within the 1.5 interquartile ranges (IQR) are mostly limited to *the polluted* condition. The value of PBLH shows greater variability under the conditions with higher PBLH, while the value of PBLH is less variable when the PBLH is low. The standard deviation of PBLH under *the good* condition is 334 m, which is almost 3 times of the PBLH standard deviation under *the polluted* condition (106 m). Deng et al. [46] performed PBLH detection during a severe haze process in November 2009 in Guangzhou, China, and found that PBLH exceeded 1 km during the cleaning process and only 500 m during the severe haze, which agree well with our results. The explanation can be associated with the

enhanced stability of urban boundary layer when the particulate matter concentration is high. Particles reduce the incoming solar radiation and lower the surface heating, leading to lower turbulent mixing and lower PBLH. PBLH will determines the level up to which the surface emissions are distributed, thus the shallow PBL further facilitate the particulate matter accumulation [23].

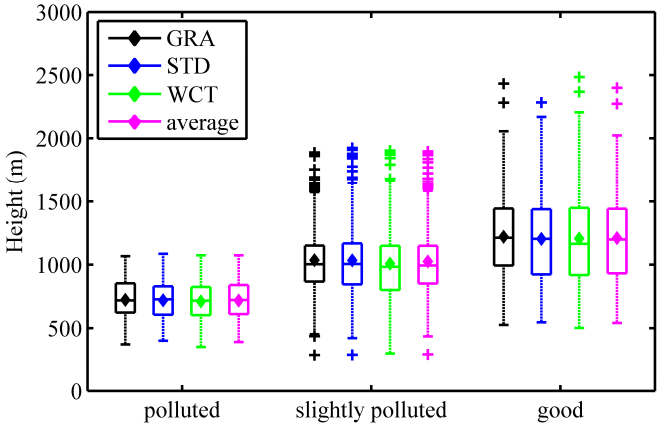

Figure 5. Average PBL height calculated by GRA, STD, and WCT methods under *good*, *slightly polluted* and *polluted* particulate pollution conditions, respectively.

Figure 6 displays the diurnal cycles of $PM_{2.5}$ concentration and PBLH from 08:00 to 20:00 under different particulate pollution conditions and their correlation. $PM_{2.5}$ concentrations are the lowest in *the good* condition, and the diurnal variation is not obvious and most of the hourly average $PM_{2.5}$ is around 23 μg/m^3. In *slightly polluted* and *polluted* conditions, the $PM_{2.5}$ level is high in both morning and evening. For *slightly polluted*, the maximum concentration of $PM_{2.5}$ is 61.43 μg/m^3, which appears at 09:00, while the greatest value of $PM_{2.5}$ in *polluted* condition occurs at 20:00 with 119.23 μg/m^3.

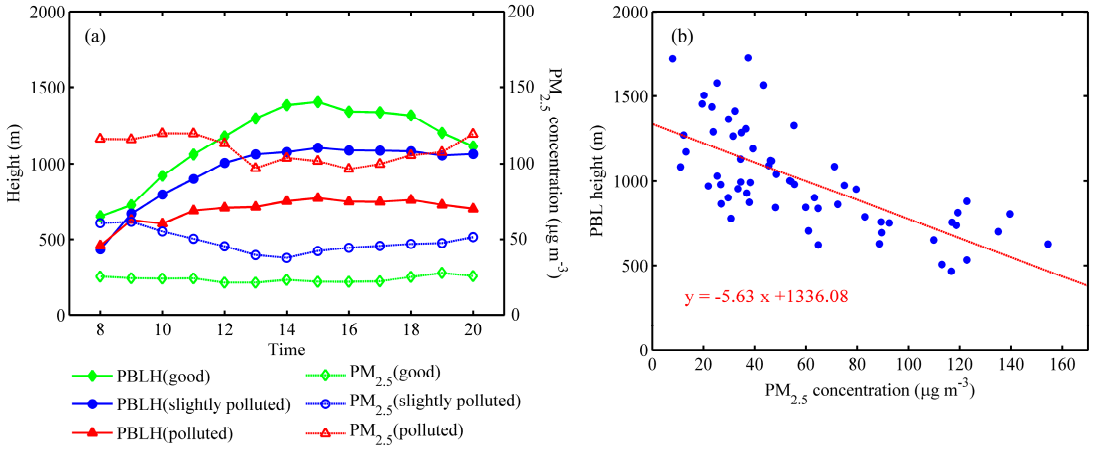

Figure 6. Diurnal variation of PBLH (three-method average) and $PM_{2.5}$ concentration under different particulate pollution conditions (**a**); and the correlation between daily average PBLH and $PM_{2.5}$ concentration (**b**). The correlation coefficient is −0.70, and the number of points is 63. The correlation is significant at the 0.01 level.

Generally, PBLH shows the opposite trend with the $PM_{2.5}$. The three conditions have comparable PBLH during the period 08:00–10:00 as well as at 20:00 of Beijing time. However, the PBLH varies a lot among different conditions in the afternoon. In *the polluted* condition, the PBLH rises from 459 m to 688 m in the first four hours, and then remains steady at around 730 m from 12:00. The PBLHs under *the good* condition exhibits the most apparent diurnal variation. It is located at 651 m at 08:00, and

then significant increase to 1405 m at 15:00. It is remains steady from 16:00 to 18:00 and then drops to 1114 m at 20:00. The general increasing trend from 08:00 to 09:00 under *the slightly polluted* condition is similar to the one under *the polluted* condition, and the PBLH remains at this level untill 20:00.

Figure 6a shows the diurnal variations of PBLH and $PM_{2.5}$ under the different pollution conditions, which indicate a negative correlation between the PBLH and $PM_{2.5}$ concentrations. Figure 6b further compares their relationship with the daily averaged PBL height and $PM_{2.5}$ concentration. The correlation coefficient is up to -0.70 and significant at the 0.01 level, which means a strong anti-correlation between the PBLH and $PM_{2.5}$. This anti-correlation can be associated with two interaction ways. On the one hand, particulate matter can change the extinction capacity of atmosphere. The increasing concentration of atmospheric particulate matter (especially fine particles) weakens the solar radiation that can reach ground. Therefore, the turbulent kinetic energy in the air close to the ground decreases and the mixing of air is not strong enough to form a higher boundary layer [56]. One the other hand, when the PBLH is relatively low, the decreasing turbulence intensity in the PBL is not conducive to the diffusion of pollutants. Thus, the $PM_{2.5}$ concentration will accumulate within the PBL. In addition, we note that the effects from the cloud, seasons and extreme weather processes can also affect the PBLH [36,53,57]. At the same time, we analyzed a case in summer, the negative correlation between the PBLH and $PM_{2.5}$ concentration are shown in supplementary Figures S2 and S3. In order to rule out the impact of these factors, we performed a case study in four consecutive days without cloud cover in Section 3.4.

3.4. Case Study

We further explore the relationship between the PBLH and $PM_{2.5}$ concentration in a selected period, which includes the development and dismiss of a particle pollution case for a continuous 4-days long. Figure 7 displays the hourly averaged PBLH, $PM_{2.5}$ concentration, wind speed, visibility, temperature and relative humidity from 14 to 17 December 2015. $PM_{2.5}$ concentration drops dramatically from 200 $\mu g/m^3$ to 30 $\mu g/m^3$ in these days. In the meantime, PBLH correlates negatively with $PM_{2.5}$ and increases from around 620 m on 14 December to 1020 m on 17 December. The transition of PBLH and boundary layer structure between 15 and 16 December can also be observed from Figure 8. On 14 and 15 December, the PBLH is relatively low with the daily average value of 627 m and 699 m, respectively. Accompanied with the low PBLH, the average wind speed is only 2.5 m/s. The shallow boundary layer and weak wind impose restrictions on the diffusion of pollutants as well as water vapor. With a high relative humidity as 71.79 % on average, aerosols are more likely to accumulate through hygroscopic formation and increase $PM_{2.5}$ concentration [58]. Thus, more particle formation and less air diffusion lead to high $PM_{2.5}$ level, which are 137.58 $\mu g/m^3$ and 155.91 $\mu g/m^3$ on 14 and 15 December, respectively. On the first two polluted days, the visibility is as low as 6 km. The strong atmospheric extinction ability due to high level $PM_{2.5}$ results in the low visibility [57]. Therefore, the radiation will be impaired through the high particulate matter loading and further against the development of boundary layer. On 16 and 17 December, the development of PBL encourages the dispersion of particulate matter. High PBLH can be observed as 1029 m on 17 December, whereas $PM_{2.5}$ decreases to 37.93 $\mu g/m^3$ on the last two days accompanied with higher wind speed and lower relative humidity. With dry clean air on 16 and 17 December, the visibility grows up to 40 km, which represents an almost six-fold increase of visibility. Growing visibility indicates the weaken extinction effect of particulate matter, and will in turn facilitate the PBL development.

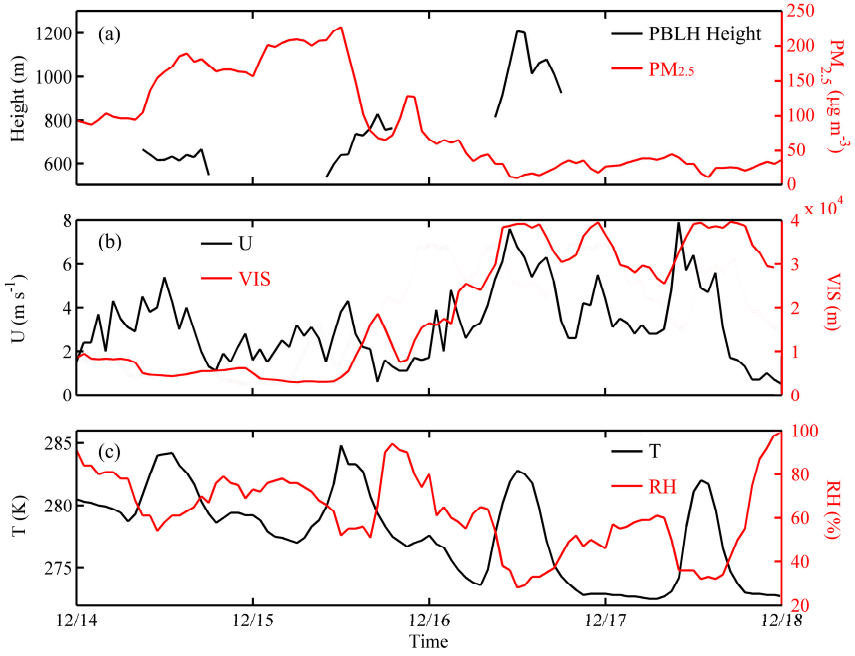

Figure 7. Time series of: (**a**) PBLH and $PM_{2.5}$ concentration; (**b**) surface wind speed (U) and visibility (VIS); and (**c**) temperature (T) and relative humidity (RH).

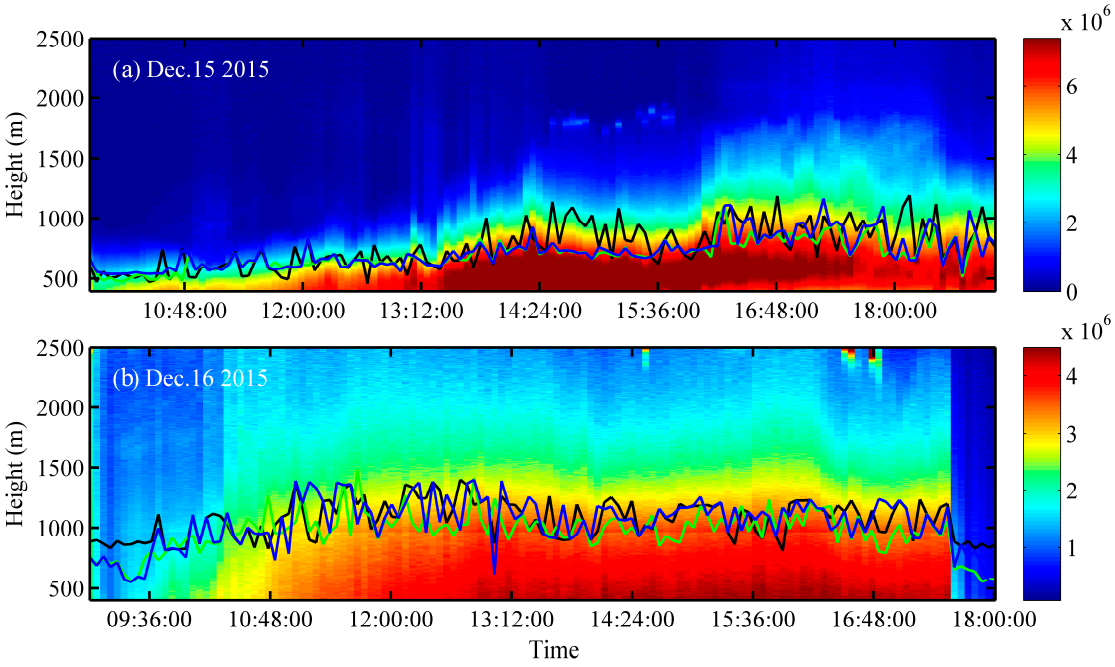

Figure 8. The diurnal variation of RCS and PBLH (calculated by three methods: black, blue and green lines represent GRA, STD and WCT method, respectively) on: 15 December 2015 (**a**); and 16 December 2015 (**b**).

4. Conclusions

In this paper, the seasonal and diurnal variations of daytime PBLH in Nanjing have been estimated from the one-year Lidar data by three different inversion methods, gradient method, standard deviation method and wavelet covariance transform method, and the correlation properties between PBLH and $PM_{2.5}$ were analyzed through both annual statistic and case study.

Generally, the three methods show consistent variation of PBLH. The PBLH estimate can be affected by the backscatter signal of boundary layer clouds, and the GRA and STD methods are all more sensitive to the signal noise than the WCT method.

Annual average PBLH in the daytime during December 2015–November 2016 in Nanjing is 992 m. The daytime PBLH shows typical seasonal trend, highest in summer and lowest in winter, and the values of which are 1351 m and 822 m, respectively. PBLH shows the maximum variability in spring, with the standard deviation of 380 m. The diurnal cycle shows similar pattern in different seasons, and for annual average diurnal variation, the minimum PBLH is 580 m, which appears at 08:00, and the maximum is 1089 m at 15:00, respectively.

The PBLH is relatively lower when the ground $PM_{2.5}$ concentration is higher. The average daytime PBLH is 718 m and 1210 m in *the polluted* condition ($PM_{2.5} > 75$ $\mu g/m^3$) and *good* condition ($PM_{2.5} < 35$ $\mu g/m^3$), respectively. The diurnal variation of PBLH is the opposite to that of $PM_{2.5}$ concentration. Daily averaged PBLH and $PM_{2.5}$ concentration are anti-correlated with a correlation coefficient of -0.70.

In the case study, $PM_{2.5}$ concentration drops from 200 $\mu g/m^3$ to 30 $\mu g/m^3$ during 14–17 December 2015 while the PBLH increases from around 620 m to 1020 m. The polluted case accompanied with the low PBLH, while the clean case shows the opposite trend (high PBLH, high visibility, high wind speed, and low relative humidity).

This study revealed the variation characteristics of PBLH and its correlation between particulate matter concentrations on the ground, based on the one-year data over Nanjing of East China. We should note that the anthropogenic emissions in Nanjing are assumed to vary little by season. The significant or large-scale weather and/or climatology processes (e.g., cold front, monsoon, El Nino, La Nina, etc.) could be important issues in further study of the PBLH variation, and requires a longer period of observations.

Supplementary Materials: The following are available online at www.mdpi.com/2072-4292/9/7/668/s1, Figure S1: Comparison of PBL-height between the (a) Lidar and (b) radiosonde measurement on 15 August 2016, Figure S2: Time series of (a) PBL height and $PM_{2.5}$ concentration, (b) surface wind speed (U) and visibility (VIS), and (c) temperature (T) and relative humidity (RH), respectively, from 14 August to 17 August 2016, Figure S3: The diurnal variation of RCS and PBLH (calculated by three methods: black, blue and green lines represent GRA, STD and WCT method, respectively) in 15 August 2016 (a) and 16 August 2016 (b).

Acknowledgments: This work was jointly supported by the National Science and Technology Major Project (grant 2016YFC0203303), the National Science Foundation of Jiangsu Province (grant BE2015151), the National Science Foundation of China (grants 41075012, 40805006, 91544230, 41675030, and 2014CB441203). Y. Wu is supported by the NOAA-CREST grant #NA11SEC481008 and NYSERDA grant #100415. We thank for DuanYang Liu from Jiangsu Meteorological Observatory for providing the meteorological data and Samuel Lightstone from the City College of New York for revising the English-writing and comments. We gratefully acknowledged the constructive comments from three anonymous reviewers that greatly improve the manuscript.

Author Contributions: Yong Han conceived the study, supervised the data analysis, and edited the manuscript. Yawei Qu performed the data analysis and prepared the manuscript. Peng Gao carried out the Lidar observation experiment to obtain the observation data. Tijian Wang provided $PM_{2.5}$ data. Yonghua Wu provided the advices and discussions on the methodology and results.

Conflicts of Interest: The authors declare no conflict of interest.

References

1. Chen, P.; Wang, T.; Lu, X.; Yu, Y.; Kasoar, M.; Xie, M.; Zhuang, B. Source apportionment of size-fractionated particles during the 2013 Asian Youth Games and the 2014 Youth Olympic Games in Nanjing, China. *Sci. Total Environ.* **2017**, *579*, 860–870. [CrossRef] [PubMed]
2. You, W.; Zang, Z.L.; Zhang, L.F.; Li, Y.; Pan, X.B.; Wang, W.Q. National-scale estimates of ground-level $PM_{2.5}$ concentration in China using geographically weighted regression based on 3 km resolution MODIS aod. *Remote Sens.* **2016**, *8*, 13. [CrossRef]

3. Artaxo, P.; Bretherton, C.; Feingold, G.; Forster, P.; Kerminen, V.M.; Kondo, Y.; Liao, H.; Lohmann, U.; Rasch, P.; Satheesh, S.K.; et al. Cloud and Aerosols. In *Climate Change 2013: The Physical Science Basis: Working Group I Contribution to the Fifth Assessment Report of the Intergovernmental Panel on Climate Change*; Cambridge University Press: Cambridge, UK; New York, NY, USA, 2014; pp. 614–623.
4. Kan, H.D.; London, S.J.; Chen, G.H.; Zhang, Y.H.; Song, G.X.; Zhao, N.Q.; Jiang, L.L.; Chen, B.H. Season, sex, age, and education as modifiers of the effects of outdoor air pollution on daily mortality in Shanghai, China: The public health and air pollution in Asia (PAPA) study. *Environ. Health Perspect.* **2008**, *116*, 1183–1188. [CrossRef] [PubMed]
5. Deng, J.J.; Wang, T.J.; Liu, L.; Jiang, F. Modeling heterogeneous chemical processes on aerosol surface. *Particuology* **2010**, *8*, 308–318. [CrossRef]
6. Park, S.S.; Jung, Y.; Lee, Y.G. Spectral dependence on the correction factor of erythemal UV for cloud, aerosol, total ozone, and surface properties: A modeling study. *Adv. Atmos. Sci.* **2016**, *33*, 865–874. [CrossRef]
7. Atwater, M.A. The radiation budget for polluted layers of the urban environment. *J. Appl. Meteorol.* **1971**, *10*, 205–214. [CrossRef]
8. Gao, Y.; Zhang, M.; Liu, Z.; Wang, L.; Wang, P.; Xia, X.; Tao, M.; Zhu, L. Modeling the feedback between aerosol and meteorological variables in the atmospheric boundary layer during a severe fog-haze event over the North China Plain. *Atmos. Chem. Phys.* **2015**, *15*, 4279–4295. [CrossRef]
9. Wang, T.J.; Li, S.; Shen, Y.; Deng, J.J.; Xie, M. Investigations on direct and indirect effect of nitrate on temperature and precipitation in China using a regional climate chemistry modeling system. *J. Geophys. Res. Atmos.* **2010**, *115*, 13. [CrossRef]
10. Attwood, A.R.; Washenfelder, R.A.; Brock, C.A.; Hu, W.; Baumann, K.; Campuzano-Jost, P.; Day, D.A.; Edgerton, E.S.; Murphy, D.M.; Palm, B.B.; et al. Trends in sulfate and organic aerosol mass in the Southeast U.S.: Impact on aerosol optical depth and radiative forcing. *Geophys. Res. Lett.* **2014**, *41*, 7701–7709. [CrossRef]
11. Wang, J.; Park, S.; Zeng, J.; Ge, C.; Yang, K.; Carn, S.; Krotkov, N.; Omar, A.H. Modeling of 2008 kasatochi volcanic sulfate direct radiative forcing: Assimilation of omi SO_2 plume height data and comparison with MODIS and CALIOP observations. *Atmos. Chem. Phys.* **2013**, *13*, 1895–1912. [CrossRef]
12. Zhuang, B.L.; Jiang, F.; Wang, T.J.; Li, S.; Zhu, B. Investigation on the direct radiative effect of fossil fuel black-carbon aerosol over China. *Theor. Appl. Climatol.* **2011**, *104*, 301–312. [CrossRef]
13. Wang, Q.Y.; Huang, R.J.; Zhao, Z.Z.; Cao, J.J.; Ni, H.Y.; Tie, X.X.; Zhao, S.Y.; Su, X.L.; Han, Y.M.; Shen, Z.X.; et al. Physicochemical characteristics of black carbon aerosol and its radiative impact in a polluted urban area of China. *J. Geophys. Res. Atmos.* **2016**, *121*, 12505–12519. [CrossRef]
14. Li, S.; Wang, T.J.; Solmon, F.; Zhuang, B.L.; Wu, H.; Xie, M.; Han, Y.; Wang, X.M. Impact of aerosols on regional climate in southern and northern China during strong/weak East Asian summer monsoon years. *J. Geophys. Res. Atmos.* **2016**, *121*, 4069–4081. [CrossRef]
15. Xia, X.; Che, H.; Zhu, J.; Chen, H.; Cong, Z.; Deng, X.; Fan, X.; Fu, Y.; Goloub, P.; Jiang, H.; et al. Ground-based remote sensing of aerosol climatology in China: Aerosol optical properties, direct radiative effect and its parameterization. *Atmos. Environ.* **2016**, *124*, 243–251. [CrossRef]
16. Zhuang, B.L.; Wang, T.J.; Li, S.; Liu, J.; Talbot, R.; Mao, H.T.; Yang, X.Q.; Fu, C.B.; Yin, C.Q.; Zhu, J.L.; et al. Optical properties and radiative forcing of urban aerosols in Nanjing, China. *Atmos. Environ.* **2014**, *83*, 43–52. [CrossRef]
17. Zhuang, B.L.; Wang, T.J.; Liu, J.; Ma, Y.; Yin, C.Q.; Li, S.; Xie, M.; Han, Y.; Zhu, J.L.; Yang, X.Q.; et al. Absorption coefficient of urban aerosol in Nanjing, west Yangtze River delta, China. *Atmos. Chem. Phys.* **2015**, *15*, 13633–13646. [CrossRef]
18. Ma, J.Z.; Xu, X.B.; Zhao, C.S.; Yan, P. A review of atmospheric chemistry research in China: Photochemical smog, haze pollution, and gas-aerosol interactions. *Adv. Atmos. Sci.* **2012**, *29*, 1006–1026. [CrossRef]
19. Huang, R.J.; Zhang, Y.L.; Bozzetti, C.; Ho, K.F.; Cao, J.J.; Han, Y.M.; Daellenbach, K.R.; Slowik, J.G.; Platt, S.M.; Canonaco, F.; et al. High secondary aerosol contribution to particulate pollution during haze events in China. *Nature* **2014**, *514*, 218–222. [CrossRef] [PubMed]
20. Tao, M.H.; Chen, L.F.; Xiong, X.Z.; Zhang, M.G.; Ma, P.F.; Tao, J.H.; Wang, Z.F. Formation process of the widespread extreme haze pollution over Northern China in january 2013: Implications for regional air quality and climate. *Atmos. Environ.* **2014**, *98*, 417–425. [CrossRef]

21. Boynard, A.; Clerbaux, C.; Clarisse, L.; Safieddine, S.; Pommier, M.; Van Damme, M.; Bauduin, S.; Oudot, C.; Hadji-Lazaro, J.; Hurtmans, D.; et al. First simultaneous space measurements of atmospheric pollutants in the boundary layer from IASI: A case study in the North China Plain. *Geophys. Res. Lett.* **2014**, *41*, 645–651. [CrossRef]
22. Stull, R.B. *An Introduction to Boundary Layer Meteorology (Vol. 13)*; Kluwer Academic Publishers: Dordrecht, The Netherlands; Boston, MA, USA; London, UK, 1988.
23. Petaja, T.; Jarvi, L.; Kerminen, V.M.; Ding, A.J.; Sun, J.N.; Nie, W.; Kujansuu, J.; Virkkula, A.; Yang, X.Q.; Fu, C.B.; et al. Enhanced air pollution via aerosol-boundary layer feedback in China. *Sci. Rep.* **2016**, *6*, 6. [CrossRef] [PubMed]
24. Zilitinkevich, S.S.; Tyuryakov, S.A.; Troitskaya, Y.I.; Mareev, E.A. Theoretical models of the height of the atmospheric boundary layer and turbulent entrainment at its upper boundary. *Izv. Atmos. Ocean. Phys.* **2012**, *48*, 133–142. [CrossRef]
25. Tyagi, S.; Tiwari, S.; Mishra, A.; Singh, S.; Hopke, P.K.; Singh, S.; Attri, S.D. Characteristics of absorbing aerosols during winter foggy period over the national capital region of Delhi: Impact of planetary boundary layer dynamics and solar radiation flux. *Atmos. Res.* **2017**, *188*, 1–10. [CrossRef]
26. Leventidou, E.; Zanis, P.; Balis, D.; Giannakaki, E.; Pytharoulis, I.; Amiridis, V. Factors affecting the comparisons of planetary boundary layer height retrievals from CALIPSO, ECMWF and radiosondes over Thessaloniki, Greece. *Atmos. Environ.* **2013**, *74*, 360–366. [CrossRef]
27. Liu, J.J.; Huang, J.P.; Chen, B.; Zhou, T.; Yan, H.R.; Jin, H.C.; Huang, Z.W.; Zhang, B.D. Comparisons of PBL heights derived from CALIPSO and ECMWF reanalysis data over China. *J. Quant. Spectrosc. Radiat. Transf.* **2015**, *153*, 102–112. [CrossRef]
28. Bianco, L.; Wilczak, J.M. Convective boundary layer depth: Improved measurement by doppler radar wind profiler using fuzzy logic methods. *J. Atmos. Ocean. Technol.* **2002**, *19*, 1745–1758. [CrossRef]
29. Munkel, C.; Schafer, K.; Emeis, S. Adding confidence levels and error bars to mixing layer heights detected by ceilometer. In *Remote Sensing of Clouds and the Atmosphere XVI*; Kassianov, E.I., Comeron, A., Picard, R.H., Schafer, K., Eds.; Spie-Int Soc Optical Engineering: Bellingham, WA, USA, 2011; Volume 8177.
30. Lotteraner, C.; Piringer, M. Mixing-height time series from operational ceilometer aerosol-layer heights. *Bound. Layer Meteorol.* **2016**, *161*, 265–287. [CrossRef]
31. Uzan, L.; Egert, S.; Alpert, P. Ceilometer evaluation of the eastern mediterranean summer boundary layer height—First study of two Israeli sites. *Atmos. Meas. Tech.* **2016**, *9*, 4387–4398. [CrossRef]
32. Casasanta, G.; Pietroni, I.; Petenko, I.; Argentini, S. Observed and modelled convective mixing-layer height at Dome C, Antarctica. *Bound. Layer Meteorol.* **2014**, *151*, 597–608. [CrossRef]
33. Petenko, I.; Argentini, S.; Casasanta, G.; Kallistratova, M.; Sozzi, R.; Viola, A. Wavelike structures in the turbulent layer during the morning development of convection at Dome C, Antarctica. *Bound. Layer Meteorol.* **2016**, *161*, 289–307. [CrossRef]
34. De Tomasi, F.; Perrone, M.R. PBL and dust layer seasonal evolution by Lidar and radiosounding measurements over a peninsular site. *Atmos. Res.* **2006**, *80*, 86–103. [CrossRef]
35. Pal, S. Monitoring depth of shallow atmospheric boundary layer to complement Lidar measurements affected by partial overlap. *Remote Sens.* **2014**, *6*, 8468–8493. [CrossRef]
36. Deng, T.; Deng, X.; Li, F.; Wang, S.; Wang, G. Study on aerosol optical properties and radiative effect in cloudy weather in the Guangzhou region. *Sci. Total Environ.* **2016**, *568*, 147–154. [CrossRef] [PubMed]
37. Wang, W.; Gong, W.; Mao, F.Y.; Pan, Z.X. An improved iterative fitting method to estimate nocturnal residual layer height. *Atmosphere* **2016**, *7*, 106. [CrossRef]
38. Hoff, R.M.; GuiseBagley, L.; Staebler, R.M.; Wiebe, H.A.; Brook, J.; Georgi, B.; Dusterdiek, T. Lidar, nephelometer, and in situ aerosol experiments in Southern Ontario. *J. Geophys. Res. Atmos.* **1996**, *101*, 19199–19209. [CrossRef]
39. Flamant, C.; Pelon, J.; Flamant, P.H.; Durand, P. Lidar determination of the entrainment zone thickness at the top of the unstable marine atmospheric boundary layer. *Bound. Layer Meteorol.* **1997**, *83*, 247–284. [CrossRef]
40. Hennemuth, B.; Lammert, A. Determination of the atmospheric boundary layer height from radiosonde and Lidar backscatter. *Bound. Layer Meteorol.* **2006**, *120*, 181–200. [CrossRef]
41. Comeron, A.; Sicard, M.; Rocadenbosch, F. Wavelet correlation transform method and gradient method to determine aerosol layering from Lidar returns: Some comments. *J. Atmos. Ocean. Technol.* **2013**, *30*, 1189–1193. [CrossRef]

42. Hooper, W.P.; Eloranta, E.W. Lidar measurements of wind in the planetary boundary-layer—The method, accuracy and results from joint measurements with radiosonde and kytoon. *J. Clim. Appl. Meteorol.* **1986**, *25*, 990–1001. [CrossRef]
43. Menut, L.; Flamant, C.; Pelon, J.; Flamant, P.H. Urban boundary-layer height determination from Lidar measurements over the Paris area. *Appl. Opt.* **1999**, *38*, 945–954. [CrossRef] [PubMed]
44. Cohn, S.A.; Angevine, W.M. Boundary layer height and entrainment zone thickness measured by Lidars and wind-profiling radars. *J. Appl. Meteorol.* **2000**, *39*, 1233–1247. [CrossRef]
45. Granados-Munoz, M.J.; Navas-Guzman, F.; Bravo-Aranda, J.A.; Guerrero-Rascado, J.L.; Lyamani, H.; Fernandez-Galvez, J.; Alados-Arboledas, L. Automatic determination of the planetary boundary layer height using Lidar: One-year analysis over Southeastern Spain. *J. Geophys. Res. Atmos.* **2012**, *117*, 10. [CrossRef]
46. Deng, T.; Wu, D.; Deng, X.; Tan, H.; Li, F.; Liao, B. A vertical sounding of severe haze process in Guangzhou area. *Sci. China Earth Sci.* **2014**, *57*, 2650–2656. [CrossRef]
47. Steyn, D.G.; Boldi, M.; Hoff, R.M. The detection of mixed layer depth and entrainment zone thickness from Lidar backscatter profiles. *J. Atmos. Ocean. Technol.* **1999**, *16*, 953–959. [CrossRef]
48. Hägeli, P.; Steyn, D.G.; Strawbridge, K.B. Spatial and temporal variability of mixed-layer depth and entrainment zone thickness. *Bound. Layer Meteorol.* **2000**, *97*, 47–71. [CrossRef]
49. Klett, J.D. Lidar inversion with variable backscatter extinction ratios. *Appl. Opt.* **1985**, *24*, 1638–1643. [CrossRef] [PubMed]
50. Du, C.L.; Liu, S.Y.; Yu, X.; Li, X.M.; Chen, C.; Peng, Y.; Dong, Y.; Dong, Z.P.; Wang, F.Q. Urban boundary layer height characteristics and relationship with particulate matter mass concentrations in Xi'an, central China. *Aerosol Air Qual. Res.* **2013**, *13*, 1598–1607. [CrossRef]
51. Schneider, J.; Eixmann, R. Three years of routine raman Lidar measurements of tropospheric aerosols: backscattering, extinction, and residual layer height. *Atmos. Chem. Phys.* **2002**, *2*, 313–323. [CrossRef]
52. Matthias, V.; Bosenberg, J. Aerosol climatology for the planetary boundary layer derived from regular Lidar measurements. *Atmos. Res.* **2002**, *63*, 221–245. [CrossRef]
53. Van der Kamp, D.; McKendry, I. Diurnal and seasonal trends in convective mixed-layer heights estimated from two years of continuous ceilometer observations in Vancouver, BC. *Bound. Layer Meteorol.* **2010**, *137*, 459–475. [CrossRef]
54. Strawbridge, K.; Travis, M.; Harwood, M. Preliminary results from scanning Lidar measurements of stack plumes during winter/summer. In Proceedings of the SPIE 4546 Laser Radar: Ranging and Atmospheric Lidar Techniques III, Toulouse, France, 17 September 2017; pp. 101–110.
55. Chinese Ministry of Environmental Protection (MEP) and General Administration of Quality Supervision, Inspection, and Quarantine (AQISQ) of the People's Republic of China. *Ambient Air Quality Standards (GB 3095-2012)*; China Environmental Science Press: Beijing, China, 2012.
56. Batchvarova, E.; Gryning, S.-E. Applied model for the growth of the daytime mixed layer. *Bound. Layer Meteorol.* **1991**, *56*, 261–274. [CrossRef]
57. Deng, J.J.; Wang, T.J.; Jiang, Z.Q.; Xie, M.; Zhang, R.J.; Huang, X.X.; Zhu, J.L. Characterization of visibility and its affecting factors over Nanjing, China. *Atmos. Res.* **2011**, *101*, 681–691. [CrossRef]
58. Levin, E.J.T.; Prenni, A.J.; Palm, B.B.; Day, D.A.; Campuzano-Jost, P.; Winkler, P.M.; Kreidenweis, S.M.; DeMott, P.J.; Jimenez, J.L.; Smith, J.N. Size-resolved aerosol composition and its link to hygroscopicity at a forested site in Colorado. *Atmos. Chem. Phys.* **2014**, *14*, 2657–2667. [CrossRef]